



# Study on the Kinetic Characteristics of Microbubbles in Cross-Shaped Flow Focusing Microchannels

Weibing Ding<sup>1,3</sup> · Qianwen Yang<sup>1,3</sup> · Yaohui Zhao<sup>1,3</sup> · Zhaohui Wang<sup>1,3</sup> · Jie Chen<sup>2</sup> · Hongxia Wang<sup>4</sup>

Received: 6 July 2023 / Revised: 17 September 2023 / Accepted: 21 September 2023 / Published online: 6 February 2024  
© The Author(s), under exclusive licence to Korean Institute of Chemical Engineers, Seoul, Korea 2024

## Abstract

To study the mechanism of microbubbles generation in cross-shaped microchannels, numerical simulations of gas–liquid two-phase flow in microchannels are carried out in this paper using the volume of fluid method (VOF). By varying the two-phase flow rate, three different flow regimes were obtained, including dripping regime, slugging regime and threading regime, and the relationship between the two-phase flow rate and the flow state was plotted. Meanwhile, the phase interface, pressure and velocity of microbubbles in three different flow regimes were studied, and the evolution of the gas–liquid interface in microbubbles formation was analyzed. It is found that the microbubbles diameter decreases and the frequency increases as the viscosity of the continuous phase gradually increases. As the wall contact angle decreases, the adhesion of the liquid phase to the wall at the channel interaction increases and the microbubbles diameter increases. The increase in interfacial tension greatly increases the cohesion between molecules on the surface of the gas flow, making it difficult to achieve force equilibrium, which leads to a reduction in the shear stress required to dominate the interface to break the tip of the gas flow and slower bubbles formation, resulting in a larger microbubbles diameter.

**Keywords** Cross-shaped channel · Flow focusing · Gas–liquid interface · Microbubbles formation · Interfacial dynamics

## Introduction

People are progressively turning their attention to microscale gadgets as a result of the rapid development of modern technology. Microbubbles are defined as bubbles with a diameter of a few microns to a few hundred microns that are not visible to the naked eye yet do exist in the actual world. Due to their special hydrodynamic properties and scale effects [1, 2], microbubbles, which are smaller, larger in surface area, and rise more slowly in water than ordinary bubbles, are

used in a variety of industries, including mineral flotation [3–5], petroleum [6], metallurgy [7], chemical industry [8], and nuclear energy [9]. Microbubbles hold great promise for use in ultrasonic molecular imagination, medicine journey and targeting treatment, and thrombus dissolution [10]. The current research on microbubbles has led to achievements in preparative techniques, diagnostic and therapeutic applications. However, there are plenty of challenges to overcome, and because the application pathway is so specialized, additional research into the process of microbubble production and the attainment of adjustable bubbles size is required to increase the utility of microbubbles in the medical and other technologically advanced fields [11].

Due to its high throughput and low cost, ultrasound is commonly used to produce microbubbles, but the frequency, power and pulse of the ultrasound generator affect the size of the microbubbles, so it is not possible to produce mono-disperse microbubbles of a specific size, when additional filtration is required to remove the larger size bubbles [12]. The mechanical mixing method prepares microbubbles by a mechanical stirrer [13], but produces microbubbles of non-uniform size. The inkjet printing method prepares microbubbles and requires the frequency or duration of pressure

✉ Zhaohui Wang  
zhwang@wust.edu.cn

<sup>1</sup> Hubei Longzhong Laboratory, Wuhan University of Technology Xiangyang Demonstration Zone, Xiangyang 441000, China

<sup>2</sup> The State Key Laboratory of Fluid Power and Mechatronic Systems, Zhejiang University, Hangzhou 310027, China

<sup>3</sup> Key Laboratory of Metallurgical Equipment and Control Technology of Ministry of Education, Wuhan University of Science Technology, Wuhan 430081, China

<sup>4</sup> College of Mechanical Engineering, Hubei University of Automotive Technology, Shi Yan 442002, China

pulses to control the size of the microbubbles [14], but is limited to the production of liquid-filled particles. The coaxial electro-fluidic atomization method is capable of producing microbubbles less than 10  $\mu\text{m}$  in diameter [15], but also produces microbubbles of uneven size. The freeze-drying method freezes the moisture content at low temperatures called ice crystals and dehydrates them after sublimation in a vacuum, it is a method with high equipment costs, a time-consuming process, high energy consumption, and so on [16]. All the above methods produce polydisperse microbubbles in liquids, but limit the potential use of microbubbles in medicine. In contrast, microfluidic techniques can produce highly monodisperse microbubbles [17].

Microfluidics has been used as a promising multidisciplinary technique for the generation of monodisperse microbubbles. It can reduce the microbubbles size by adjusting the flow parameters and reducing the orifice structure to produce microbubbles of sufficiently small size. Microfluidics has the advantages of high controllability, small sample size and low cost. The types of microfluidic channels commonly used for microbubbles formation can be classified into three types: T-type, coaxial flow type and flow focused type. The T-type connector device has a simple structure consisting of a liquid channel, and a gas channel that vertically crosses with the liquid channel [18]. For the general T-type structure, the formation of microbubbles with diameters less than 10  $\mu\text{m}$  is still problematic [19]. Coaxial flow devices usually have an exit orifice wider than the microbubbles diameter and the liquid velocity is large enough so that the dominant force for microbubbles formation is liquid inertia. Coaxial flow devices are characterized by a thin capillary tube supplying the gas, which is surrounded by a coaxially arranged capillary tube supplying the liquid [20]. Flow focusing microchannels typically consist of a central gas channel, two lateral liquid channels, and a narrow exit orifice [21]. Flow focusing microchannels use a constricted orifice downstream of the inlet of the dispersed phase to modify the hydrodynamic behavior of the flow field and thus the formation of microbubbles. Compared with other microchannels, microbubbles formation in flow focusing microchannels is more controllable, and the generated bubbles are relatively stable, monodisperse, and have a wide range of adjustable sizes, thus attracting extensive attention and research from researchers.

There are many studies on the formation of microbubbles in flow focusing microchannels up to now. Yu et al. [22] studied droplets formation in microchannels with different divergence angles by visualization experiments. Four flow regimes of the fluid in the channel were observed: squeezing, dripping, jetting and threading, and then the droplet formation mechanism was analyzed, and finally a flow diagram was provided to describe the droplets

formation at different divergence angles. Roumpea et al. [23] used experiments to study the formation of water droplets in organic continuous phase when there is surfactant in flow focusing microchannels, and four flow regimes were identified: squeezing, dripping, jetting and threading. When surfactant is present, the two-phase flow boundary in the channel changes. For all solutions studied, three phases of droplet formation were identified: expanding, necking and pinch-off. Huang et al. [24] studied two-phase flow in crossed channels controlled by liquid-phase flow rate and gas-phase pressure to obtain flow phase diagrams of gas–liquid two-phase flow in microfluidic channels. And the relationship between the inlet conditions (including gas-phase pressure and liquid-phase flow rate) and the gas flow pattern in the microchannel was investigated in depth. Han et al. [25] divided the droplets formation into three stages: filling stage, necking stage and separation stage. Droplet formation relies mainly on the shear of the continuous relatively dispersed phase. Among them, the two-phase flow rate ratio, continuous phase viscosity and interfacial tension are the critical factors affecting droplets size and frequency. As the flow rate ratio increases, the droplets size becomes larger and the frequency decreases. As the viscosity of the continuous phase increases, the droplets size becomes smaller and frequency increases. When the interfacial tension between the two phases increases, the droplets size becomes larger and the frequency decreases. Sontti et al. [26] developed a computational model to determine the state and transition of droplet formation in a square microfluidic flow focusing device to finally obtain the droplet shape, size and formation frequency. The effects of various physicochemical parameters on droplets dynamics and flow regime transition were also systematically investigated to develop flow diagrams for different flow regimes based on the droplets formation mechanism. Pan et al. [27] analyzed the effect of channel size on droplet survival by investigating the preparation of S/W composite droplets in a vertical T-shaped channel, and found that both tube length and oil phase flow rate have an effect on droplet viability, and both conditions need to be controlled to obtain high throughput sulfur/water composite droplets. Ngo et al. [28] investigated droplets formation in double T-shaped microchannels based on the volume of fluid method and concluded that droplet formation was significantly related to the viscosity ratio of the two phases, and the droplets size decreased and the flow pattern shifted as the viscosity ratio increased.

The study of bubbles formation in microchannels now has been extended from single to multiple channels to analyze the mechanism of bubbles formation. Hashimoto et al. [29] investigated bubbles and droplets formation in single and multiple channels and found that the kinetic difference between bubbles and droplets formation originated from the compressibility of the dispersed phase, and the

droplets or bubbles formation process in the case of low capillary number was related to the continuous phase fluid pressure. Mi et al. [30] obtained the flow pattern transition of gas–liquid two-phase flow in the channel by studying bubbles formation in a high-viscosity liquid in a step-emulsification device, the transition between flow patterns could not be observed in a low-viscosity liquid. Zhang et al. [31] studied the bubbles formation mechanism in a multi-parallel microchannel using a high-speed camera, and obtained the gas–liquid interface by observing the evolution of the gas–liquid interface. The evolution is controlled by inertial force, viscous force, pressure difference between the two phases of fluid and Laplace pressure. Zhang et al. [32] observed bubbles formation in a step-emulsification microdevice via a two-angle photography method and studied the relationship between gas–liquid flow rate, liquid viscosity and other parameters on bubbles size, CV and bubbles formation phase period, it was found that the bubbles size in a certain range is independent of gas–liquid flow rate and in that range. Zhan et al. [33] investigated the effect of gravity and buoyancy on bubbles formation by varying the placement of the step-emulsification microdevice. It was found that in horizontally placed microchannels, buoyancy promotes bubble pinch-off and the effect of gravity on pinch-off can be neglected. Ma et al. [34] observed the breakup and distribution of droplets in the T-junction channel using a high-speed camera, and the droplet volume distribution ratio tended to decrease and then increase as the Reynolds number of the continuous phase increased, and the viscosity of dispersed phase had a weaker effect on the droplets breakup process than the interfacial tension.

In this paper, a two-dimensional numerical model of microbubbles formation in flow focusing microchannels is developed using the VOF method, and the effects of these parameters on microbubbles formation are investigated by varying the physical properties and flow rates of the two-phase fluids. The effects of the two-phase flow state, physical properties of the immiscible fluid (including flow rate ratio, viscosity and interfacial tension) and wall wettability are comprehensively analyzed.

## Model Description

### Flow Focusing Microchannel Structure

As shown in Fig. 1(a), a three-dimensional model view of the flow focusing microchannel is shown, with microbubbles formed by the extrusion break of focusing structure, and a clearer description of the whole is provided by the presentation of this three-dimensional structure. The upper part of the three-dimensional structure is expanded as shown in Fig. 1(b), which is axisymmetric and includes boundary conditions and

geometry. It mainly consists of two velocity inlets and one outlet, with a dispersed phase inlet velocity of  $U_d$  and a continuous phase inlet velocity of  $U_c$ . In addition, the geometry is defined by six parameters including orifice width ( $W_d/2$ ), continuous phase inlet constriction width ( $W_{c1}$ ), continuous phase inlet width ( $W_{c2}$ ), outlet width ( $W_{out}/2$ ), constriction angle ( $\alpha$ ) and extension angle ( $\beta$ ), where  $W_d$  is 2  $\mu\text{m}$ ,  $W_{c2}$  = 4  $\mu\text{m}$ ,  $W_{c1}$  = 1.8  $\mu\text{m}$ ,  $W_{out}$  = 5.2  $\mu\text{m}$ ,  $\alpha$  = 10°,  $\beta$  = 5°, and geometrical structure parameters from the literature [35]. The gas phase inlet is located  $L_1 = 2W_d$  upstream from the orifice and the liquid phase inlet is located  $L_2 = 2W_{c2}$  from the constriction to allow the flow to fully develop before entering the orifice. The exit channel is located at  $L_3 = 15W_d$  from the end of the outlet expanding angle to ensure that the two-phase flow is fully developed in the downstream microchannel. Three pressure detection points are set at the center of the three focusing holes: d, c and p. The disperse phase extension length at the focusing hole structure is defined as  $L_{tip}$ , which is subsequently measured by Image J software for related studies. Figure 1(c) shows the mesh division with local magnification at the focusing holes, where the squeezing effect of the continuous relative dispersed phase can be seen, generating microbubbles by squeezing.

### Numerical Model

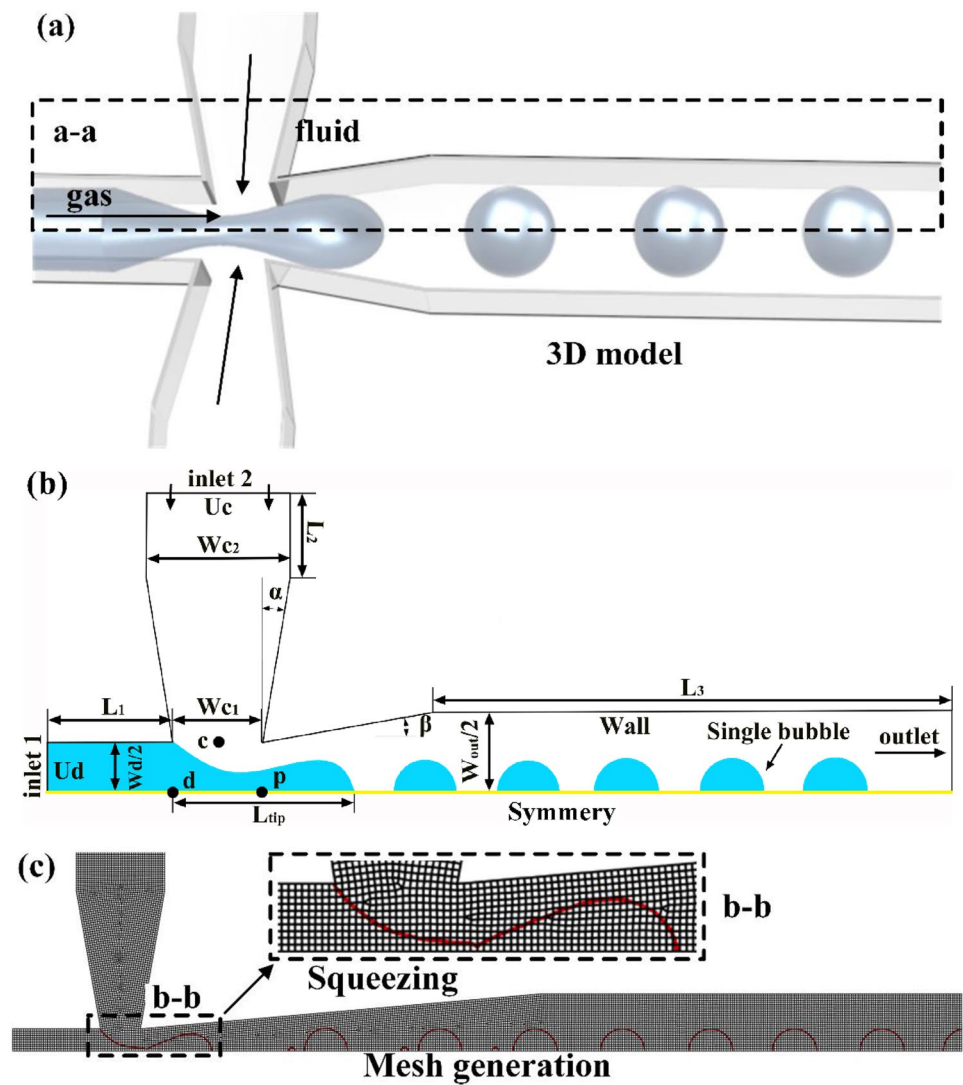
The Reynolds number ( $Re_c = \rho_c u d_h / \mu_c$ , where  $\rho_c$  and  $\mu_c$ , respectively represent the density and viscosity of the continuous phase and  $d_h$  represents the hydraulic diameter of the system) in all cases of the flow focusing system is less than 10 [36]. Therefore, fluid flow can be regarded as laminar flow. In this paper, the VOF method is used to track the interface between the continuous phase and the dispersed phase. Since the density and viscosity of the two-phase fluid are constant, it can be regarded as an incompressible isotropic Newtonian fluid. In order to study the flow characteristics of incompressible fluid in the channel more accurately, the influence of heat transfer and gravity are not considered in the channel. Therefore, the governing equation of the Navier–Stokes equation describing the momentum conservation is shown as follows

$$\nabla \cdot \boldsymbol{\nu} = 0 \quad (1)$$

$$\frac{\partial \boldsymbol{\nu}}{\partial t} + (\boldsymbol{\nu} \cdot \nabla) \boldsymbol{\nu} = -\frac{1}{\rho} \nabla P + \frac{1}{\rho} \mu \nabla (\nabla \boldsymbol{\nu} + \nabla \boldsymbol{\nu}^T) + \frac{1}{\rho} \mathbf{F}_{st} \quad (2)$$

where,  $\boldsymbol{\nu}$  is the velocity vector of the fluid;  $t$  is time;  $P$  is pressure;  $\rho$  and  $\mu$  are the density and dynamic viscosity of the fluid, respectively.  $(\boldsymbol{\nu} \cdot \nabla) \boldsymbol{\nu}$  is the inertia force per unit volume of fluid;  $\nabla P$  is the pressure gradient per unit volume of fluid;  $\mu \nabla (\nabla \boldsymbol{\nu} + \nabla \boldsymbol{\nu}^T)$  represents the viscous force per unit volume of fluid. In a two-phase mixing unit, the calculation

**Fig. 1** (a) Schematic of the droplet generation in a 3D flow focusing microfluidic device, (b) the axisymmetric 2D flow focusing structure and boundary conditions settings, and (c) the geometry of mesh division



of two-phase mixing density and viscosity in Eqs. (1) and (2) can be obtained from Eqs. (3) and (4)

$$\rho = \varphi_d \rho_d + \varphi_c \rho_c \tag{3}$$

$$\mu = \varphi_d \mu_d + \varphi_c \mu_c \tag{4}$$

$F_{st}$  is the momentum source term associated with surface tension, this force can be calculated using Continuum Surface Force (CSF) model proposed by Brackbill et al. [37], as follows:

$$F_{st} = \sigma \kappa \nabla \varphi \tag{5}$$

where,  $\sigma$ ,  $\kappa$  and  $\nabla \varphi$  denote the surface tension coefficient, the curvature of interface, and the normal direction with respect to the droplet surface.

$$\kappa = \nabla \cdot \hat{n} \tag{6}$$

where,  $\hat{n} = \frac{\vec{n}}{|\vec{n}|}$ ,  $\vec{n} = \nabla \varphi$ .

The capture of two-phase interfacial motion can be characterized by calculating the distribution of the volume fractions  $\varphi_c$  and  $\varphi_d$  of continuous phase and dispersed phase in a grid cell, Where,  $\varphi_c=1$  and  $\varphi_d=0$  represent continuous phase,  $\varphi_d=1$  and  $\varphi_c=0$  represent dispersed phase. Therefore, two intersecting interfaces in a cell depend on the values between 0 and 1 of  $\varphi_c$  and  $\varphi_d$ . The sum of volume fraction of all fluids is:

$$\varphi_c + \varphi_d = 1 \tag{7}$$

A transport equation for  $\varphi_c$  is solved to track the evolution of liquid–liquid interface, as follows:

$$\frac{\partial \varphi_c}{\partial t} + \mathbf{v} \cdot \nabla \varphi_c = 0 \tag{8}$$

In a computational grid adjacent to the wall, two phases of liquid and gas contact the wall at a fixed angle, and the influence of the wettability of the wall can be characterized by the contact angle model. The contact angle  $\theta$  can be defined as the angle between the liquid–gas interface and the solid–liquid interface at the interface of solid wall, liquid phase and gas phase. In this model, the unit normal vector in the cell close to the wall can be obtained by Eq. (9).

$$\hat{n} = \hat{n}_w \cos \theta + \hat{t}_w \sin \theta \tag{9}$$

$\hat{n}_w$  and  $\hat{t}_w$  represent the wall unit normal vector and the tangent vector.

In addition to the governing equation, the relevant boundary conditions of the flow focusing microchannel are as follows: both phases are uniform inlet. Take the ambient pressure as the reference pressure of the outlet fluid, equal to 0 Pa. The contact angle was set as  $50^\circ$ , and the channel wall was set as no slip boundary condition.

### Numerical Solutions

In this study, a double precision pressure solver was used for numerical simulation. A PISO algorithm (an implicit pressure algorithm with operator splitting) is used to achieve horizontal pressure coupling, which is based on the higher order of the approximate relationship between pressure and velocity correction. PRESTO was selected as the pressure interpolation algorithm, the momentum term was in the second-order upwind form, and the volume fraction was in the geometrically reconstructed form. Because of the high precision of curvature calculation, geometric reconstruction schemes are used for interfacial interpolation.

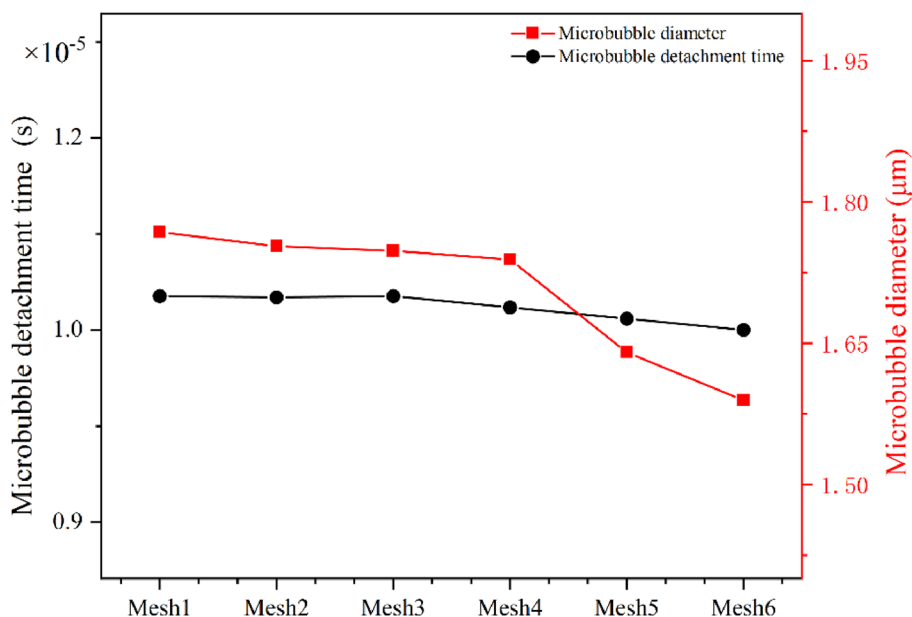
The convergence criterion is  $1 \times 10^{-6}$ . In the simulation, the variable step size is automatically adjusted according to the criterion that the global Courant number is less than 0.25, so as to maintain the stability and convergence of the solution. The commercial package ANSYS Fluent 19.0 was used in the transient numerical simulations in this study, and all boundaries were assumed to be adiabatic.

### Mesh Independence and Model Validation

Generally, within a certain range, the smaller the grid, the more accurate the calculation result. However, the smaller the mesh, the more computing resources it consumes. To obtain the most economical mesh size, a two-dimensional geometric model of unstructured mesh convective focusing microchannels is used for mesh partitioning. Since different design variables will have an impact on the number of mesh, six scale sizes, from mesh 1 to mesh 6 (mesh size increases gradually, the minimum mesh size is  $5 \times 10^{-5} \mu\text{m}$ , maximum mesh size is  $2 \times 10^{-4} \mu\text{m}$ ), are selected for mesh division. As shown in Fig. 2, from mesh1 to mesh6, the change between the minimum and maximum values of microbubble fracture time is 0.55%, indicating the requirement of full precision of mesh cells. However, the diameter of microbubbles decreases sharply from mesh5, indicating that the large mesh size leads to an increase in the error of calculation. Therefore, mesh3 was chosen as the mesh size for the geometric channels in the subsequent simulations to balance the accuracy of calculation results with the expense, and the mesh size is  $1 \times 10^{-4} \mu\text{m}$ .

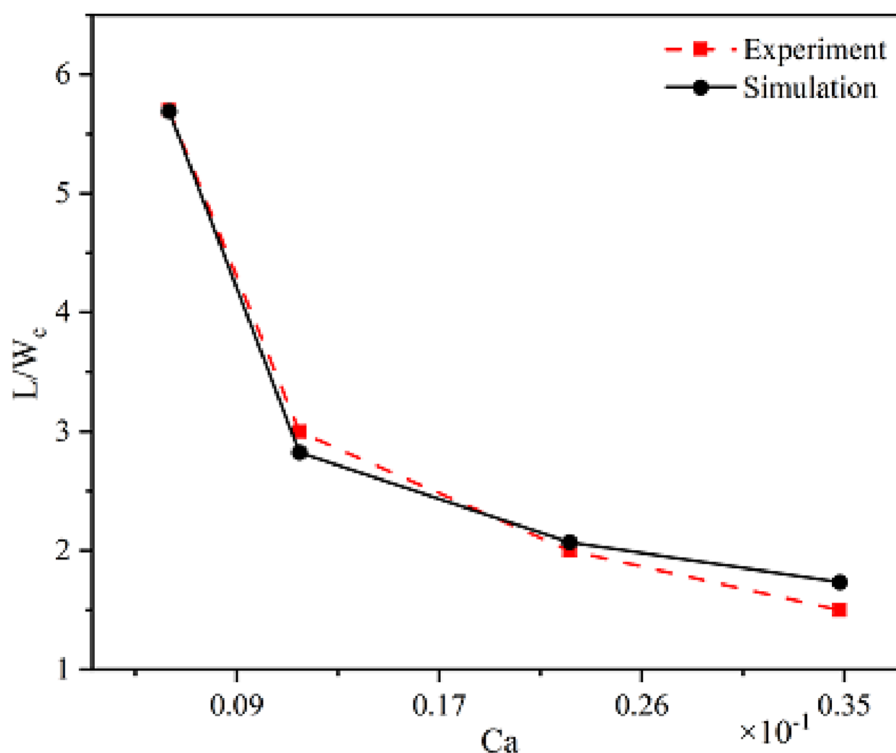
In addition, to verify the accuracy of the current numerical simulation calculation method, the numerical

Fig. 2 The result of mesh independence verification





**Fig. 3** Comparison of numerical results of dimensionless micro-bubble size with experimental results



simulation results were compared with the experimental results in the literature [38]. As shown in Fig. 3,  $L$  is the length of slug bubble, it can be seen from the figure, the microbubble formation results obtained by numerical simulation are in good agreement with the experimental results, and the average error of simulated value and the experimental value is 6.27%, which is within the acceptable range. Therefore, it can be concluded that the numerical simulation method used in this paper is accurate and feasible to characterize the two-phase flow patterns in cross-shaped microchannels.

## Results and Discussion

It has been shown in various studies that bubble formation in microchannels is also influenced by flow rate, density, viscosity, wall wettability and interfacial tension. A systematic analysis of the factors influencing microbubble generation can be carried out through the advantage of numerical methods that allow flexible parameter changes.

### The Effect of Two-Phase Flow Velocity

Water was chosen as the continuous phase (with a density and viscosity coefficient of  $\rho_c = 1000 \text{ kg/m}^3$ ,  $\mu_c = 1.0 \text{ mPa}\cdot\text{s}$ ), nitrogen as the dispersed phase (with a density and viscosity coefficient of  $\rho_d = 1.138 \text{ kg/m}^3$ ,  $\mu_d = 0.01663 \text{ mPa}\cdot\text{s}$ )

and a surface tension coefficient between the two phases of  $\sigma = 0.072 \text{ N/m}$ . The straight channel carries the gas phase ( $\text{N}_2$ ) and the liquid phase flow (Water) is permeated into the main channel in the region of the conjunction. At the conjunction, the gas phase is transformed into bubbles. At the end of the rupture process, the resulting bubbles flows in the straight channel to the outlet.

Variations in the continuous phase inlet velocity and the dispersed phase inlet velocity can change the competition of the controlling forces involved in microbubble generation in the microfluidic cross-junction, which gives rise to three different microbubble flow patterns. Therefore, based on the numerical results of this study, the flow patterns of microbubbles are plotted for different continuous and dispersed phase inlet flow rates to quantitatively represent the three flow patterns of microbubble formation.

Figure 4(a) represents three flow patterns of microbubbles in a microchannel for gas–liquid phase flow by means of mapping the surface velocity of the two phases: dripping regime, plugging regime and threading regime. When  $U_d$  becomes significant, the gas flow in the channel is dominated by the Threading regime. The plugging regime appears at smaller  $U_c$ . The dripping regime appears more widely, occupying more than half. The three different flow regimes of microbubbles in the channel are represented in Fig. 4(b) using in cloud diagrams.

In the dripping regime (Fig. 4b–i), the gas flow in the microchannel can largely obstruct the fluid flow at the

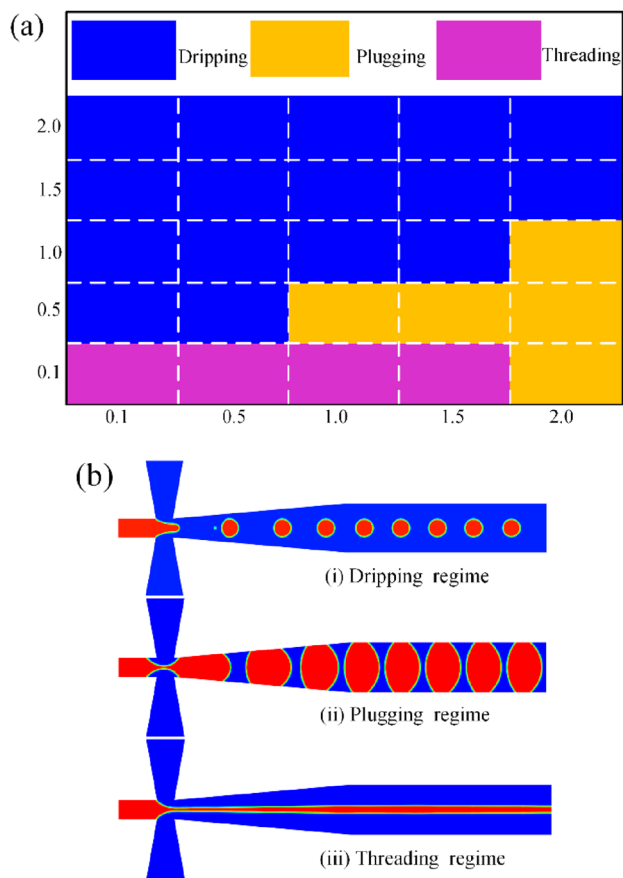


**Fig. 4** (a) Gas–liquid flow regime of an improved flow focusing microchannel obtained from  $U_d$  and  $U_c$ ; (b) Three flow regimes of fluids in microchannels: (i)-Dripping regime ( $U_d/U_c=1$ ); (ii)-Plugging regime ( $U_d/U_c=10$ ); (iii)-Threading regime ( $U_d/U_c=2$ )

orifice. The continuous phase is supplied continuously from the two side inlets at right angles to the central inlet, resulting in a pressure accumulation in the gas phase at the orifice, which squeezes the gas flow. As the gas line is thread-necked, interfacial tension increases to hold on to the gas flow. When the interfacial tension is overcome by the squeezing pressure and the viscous shear that is applied by the continuous phase, the gas flow line breaks off into microbubbles, releasing the squeezing pressure and repeating the process. Sometimes the filaments connecting the gas stream to the microbubbles form satellite microbubbles. However, the satellite bubbles quickly catch up with the main bubble and flow towards the end of it and merge with it.

In the plugging regime (Fig. 4b–ii), the formation of microbubbles has similarities to the dripping regime, but more gas is dispersed into the main channel, forming the segment plug. The segment plug bubbles contact the microchannel walls and move along the microchannel. The flow situation in which the microbubbles remain in contact with the side walls is the segment plug state. The viscous

shear and drag from the continuous phase, and the fact that the inertia of the dispersed phase is so small, allows the dispersed phase to follow a swelling process at the orifice, controlled by interfacial tension, and thus also a subsequent squeezing and necking process.

In the threading regime (Fig. 4b–iii), the continuous phase flows as a gas flow in the main channel with less interface deformation. At the interface, the inertia of the gas is less than that of the liquid, and it is difficult to see how the gas–liquid interface tends to favor the water channel on either side. At higher dispersed phase flow rates, the squeezing pressure of the continuous phase is not sufficient to overcome the surface tension in a short time to force the gas phase to break off to the formation of microbubbles. When  $U_d$  is further increased, a cascade state emerges, as shown in Fig. 4(b–iii). In this case, the inertia of the dispersed phase is large enough to produce a uniform and steady flow of gas downstream and no microbubbles are generated during the cascade. It can be concluded that the inertial force of the dispersed can weaken the effect of interfacial tension and thus suppress the Rayleigh-Plateau instability. As a result, gas flow fluctuations and fractures do not occur.

Figure 5 shows the bubbles formation process in the dripping regime in a microchannel, including (a) the two-phase flow interface, (b) the pressure and (c) the evolution of velocity with time. The microbubbles formation process in the dripping regime can be divided into: expanding, squeezing, necking and pinch-off. In the initial phase of bubbles formation, as in Fig. 5(a) at  $t=0.8 \mu\text{s}$ , this is when the gas flows slowly downwards from the inlet and does not extend to the sides of the channel. As the gas flow passes through the continuous phase channel, it is sheared by the continuous phase fluid and necked off by the contracting structure of the channel, as shown in Fig. 5(a) at  $t=1.5 \mu\text{s}$ . After the necking phase, high pressure zones appear on either side of the neck and this pressure difference causes the gas flow to change from contraction to pinch-off, as shown in Fig. 5(a) at  $t=1.6 \mu\text{s}$ , at which point the corresponding velocity decreases. It is observed from the whole figure that the breaking of the microbubbles occurs at the junction of two-phase flow, and as the exit part of channel changes from narrow to wide, this change makes the channel have a flow focusing effect and the diameters of microbubbles obtained are all smaller than the width of channel, at which point a string of uniformly sized monodisperse bubbles is obtained.

The results show that the channel is plugging regime at small  $U_c$ . Figure 6 shows the evolution of the two-phase flow-phase interface, pressure field and velocity field in microbubble formation in the plugging regime with time. As shown in the Fig. 6, the microbubble formation process in the plugging regime can be divided into four stages: expanding, squeezing, necking and pinch-off. During the

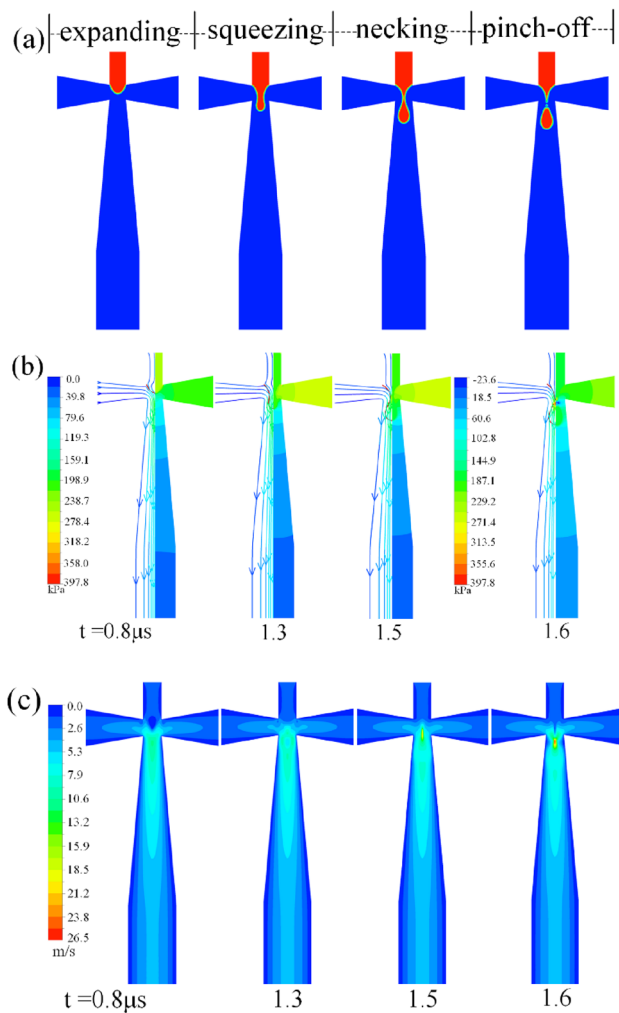


**Fig. 5** Time evolution of hydrodynamic information during microbubbles formation in an improved microchannel (dripping regime): (a) evolution of interface profile for bubbles formation; (b) pressure field and flow field; (c) velocity field

expanding phase (see  $t = 1.51\text{--}2.211\ \mu\text{s}$  in the Fig. 6), the early part of the dispersed phase tip remains expanded and spherical at the junction as the shear and squeeze of continuous phase is much smaller than the interfacial tension at small  $U_c$ , with the continuous injection of the dispersed phase. As the volume of the front portion increases, the gap between the interface and the corners of main and side channels decreases, limiting the flow of continuous phase into the downstream main channel. As a result, the pressure in the side channels increases, creating a “compression pressure” in the dispersed phase. Once this pressure is high enough to control the interfacial tension, it starts to squeeze the front end towards the center line of main channel in which the squeezing phase begins. During the squeezing phase (see  $t = 2.21\text{--}2.91\ \mu\text{s}$  in the Fig. 6), the gas flow tip thins and gradually blocks the outlet of jointed region. When the

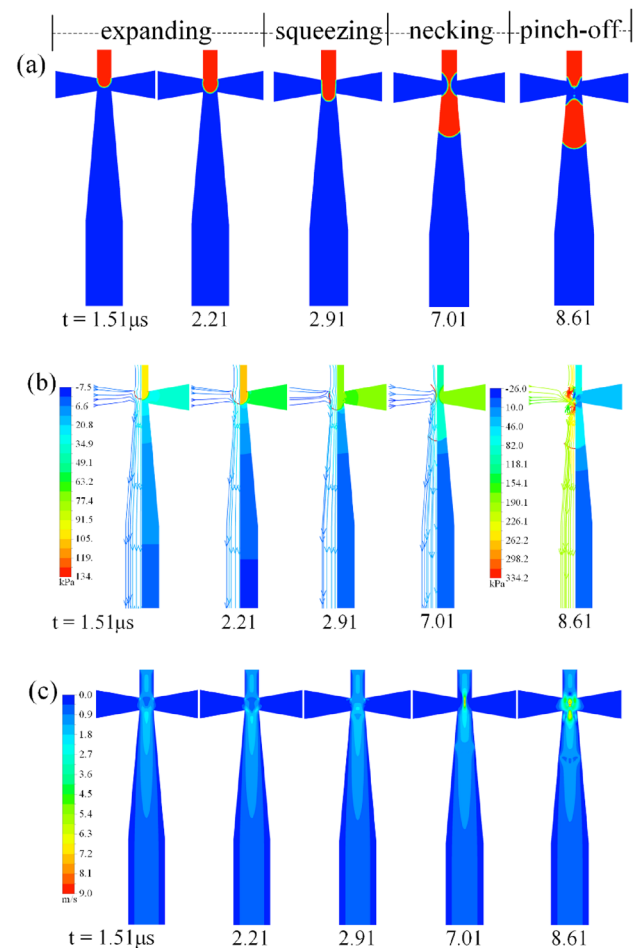


**Fig. 6** Time evolution of hydrodynamic information during microbubbles formation in an improved microchannel (plugging regime): (a) evolution of interface profile for bubble formation; (b) pressure field and flow field; (c) velocity field

convex interface at the front of the gas flow is completely flattened, the interface evolves into the necking phase. At this stage (see  $t = 2.91\text{--}7.01\ \mu\text{s}$  in the Fig. 6) the gas flow interface becomes concave and a visible neck is formed at the junction zone. The necking continues as the line is extended downstream by the coupling of the “compression pressure” and the advance of the dispersed phase from upstream. At this stage, the dispersed phase of the neck flows downstream. When the minimum size of the neck is reduced to the height of the channel, the microbubbles formation process enters the pinch-off phase (see  $t = 7.01\text{--}8.61\ \mu\text{s}$  in the Fig. 6). In the early stage of pinch-off, the neck is out of contact with the inner wall of the channel and is completely surrounded by the continuous phase. In the late pinch-off phase, a high pressure zone appears within the neck due to the presence of a large Laplace pressure difference at the neck interface with a large axial curvature (see  $t = 8.61\ \mu\text{s}$  in Fig. 6(b)).



When the velocity of continuous phase is greater than the velocity of dispersed phase, as shown in Fig. 7, the gas flow goes through four stages at this point: expanding, squeezing, necking and extending. As the velocity of dispersed phase increases, the gas flow in the channel increases, and squeezing occurs when the gas flow is sheared as it moves into the continuous phase channel, as shown in Fig. 7 at  $t = 1.3 \mu\text{s}$ . In the necking stage, due to the increase in volume of the first half of gas flow, although squeezed by the channel structure, the gas flow cannot be sheared after passing through the necking stage due to the increased inertia of dispersed phase, and eventually only flows out as a threading. As shown in Fig. 7(b), the pressure developed as the gas

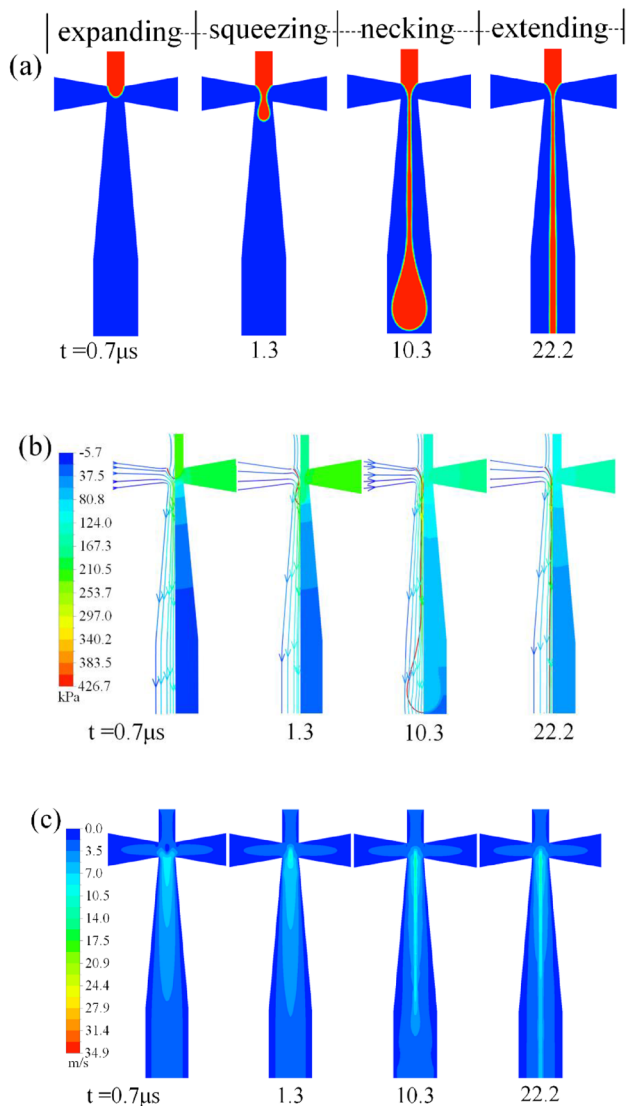


**Fig. 7** Time evolution of hydrodynamic information during microbubbles forming in an improved microchannel (threading regime): (a) evolution of interface profile for threading formation; (b) pressure field and flow field; (c) velocity field

flow goes through the necking stage cannot overcome the interfacial tension, and the gas flow tip can only be dragged downwards, so that no breakage of the threading occurs.

Figure 8 represents the variation of microbubbles diameter and generation frequency by varying the velocity of the two phases in the dripping and plugging regime, here it refers to the bubbles formed in the channel. As can be seen in Fig. 8(a), the diameter of microbubbles increases with higher velocities of dispersed phase and the diameter of microbubbles with lower velocities of the continuous phase. From Fig. 8(b), it can be seen that the higher velocity of continuous and dispersed phases, the higher frequency of microbubble formation.

The evolutionary properties of the gas–liquid interface can be used to describe the mechanisms of microbubbles formation. The evolution of interface is often represented by two characteristic values: one is the tip distance of the

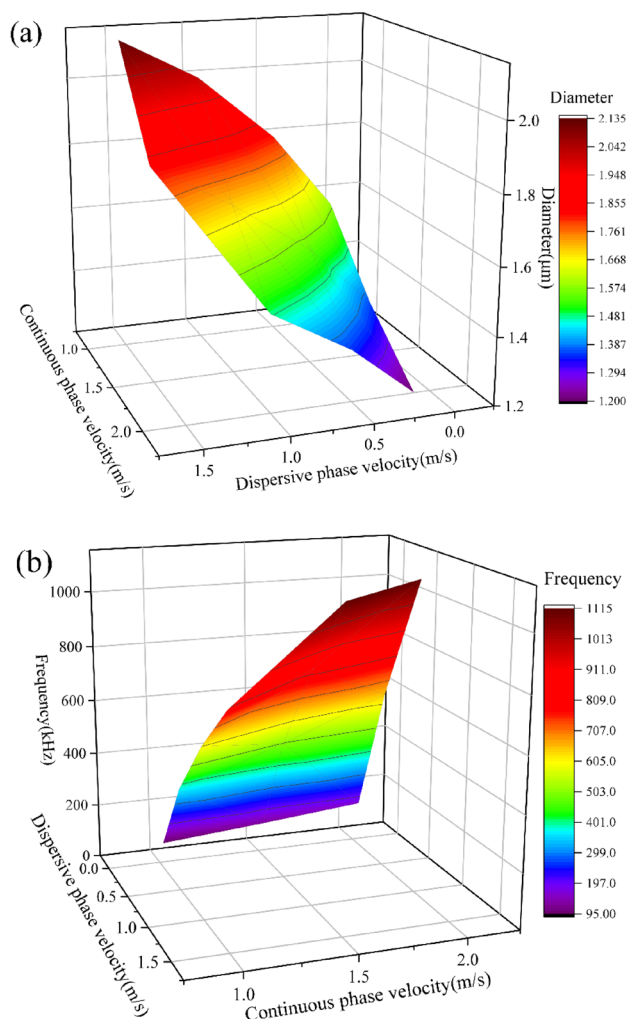


**Fig. 8** Results of microbubble forming at different continuous and dispersed phase flow rates: (a) microbubble diameter; (b) frequency of microbubble formation

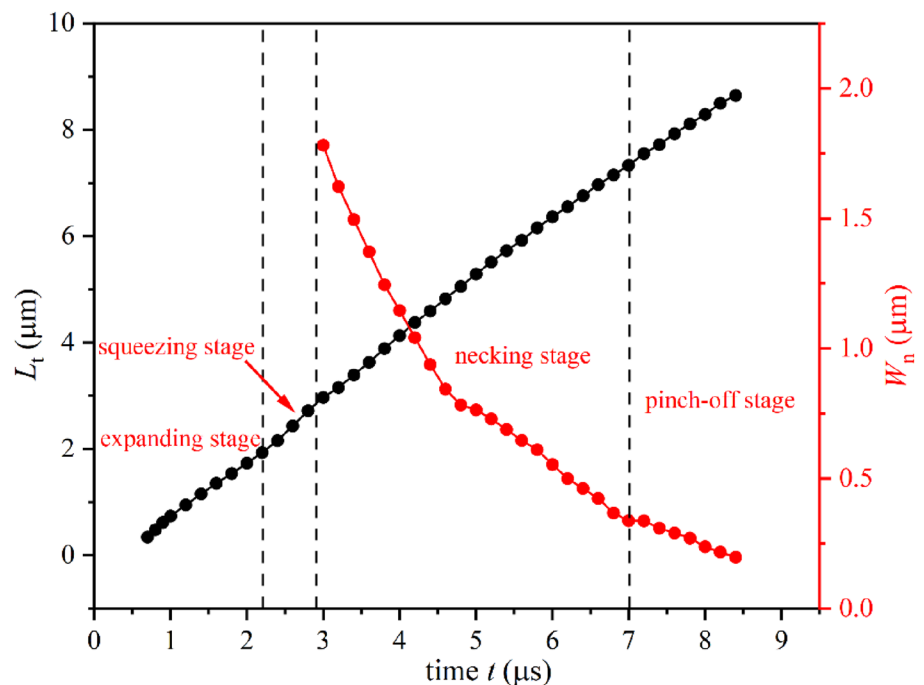
gas-phase flow, represented by  $L_t$ , and the other is the neck width, represented by  $W_n$ . To quantify the dynamics of this process, the slopes of the changes in the characteristic quantities,  $dL_t/dt$  and  $dW_n/dt$ , are plotted. As shown in Fig. 9, we define the neck width of a bubble as  $W_n$  during the generation of a microbubble.

The evolution of the tip distance of the gas flow versus the neck width is shown in Fig. 9. The tip distance of the gas flow shows a non-linear increasing trend with time. The variation of  $L_t$  and  $W_n$  with time during microbubbles formation is given in Fig. 9, from which it can be seen that during the expanding phase,  $L_t$  changes very little and the slope of the curve is 2. During the expanding phase,  $L_t$  gradually increases and the tip distance grows to a maximum value of  $1.934 \mu\text{m}$  during the expanding phase, which is due to the fluid restriction of the channels on both sides, and the microbubbles grow mainly in the axial direction. As the gas continuously enters the orifice and enters the squeezing stage, the curvature of the side of the microbubbles gradually approaches zero, and the growth rate of the tip of the microbubbles increases, and the growth distance in the squeezing stage is  $0.786 \mu\text{m}$ . When the neck occurs, the bubbles forming process enters the neck shrinkage stage, and at this time in the neck of the microbubbles, the pressure of the liquid phase is greater than the pressure of the gas phase, and the neck starts to be concave, and the initial value of neck width is  $1.782 \mu\text{m}$ , and with the passage of time, the neck width gradually decreases to  $0.338 \mu\text{m}$  and the rate of decrease gradually slows down. It can be seen that the necking stage accounts

for nearly half of the whole cycle, this is because during the necking process, the continuous phase enters the inlet of dispersed phase, resulting in a greater curvature of the neck, thus weakening the compression of continuous phase against the neck of dispersed phase and slowing down the necking process. When entering the rapid breakage stage, the tip distance continues to increase to reach a maximum value of  $8.648 \mu\text{m}$ , and the width of the bubble neck decreases rapidly with a constant rate of decrease. The rate of change of the bubbles neck width is decreasing, while the rate of change of the bubble tip length is not significant in each phase.

Figure 10 shows the effect of different flow rates of the continuous and dispersed phases on  $L_t$  and  $dL_t/dt$  during the formation of microbubbles. From Fig. 10(a), when  $U_d/U_c=0.5$ , the average velocity of the microbubbles tip  $L_t$  growth is  $1.29 \mu\text{m}/\mu\text{s}$ , and when  $U_d/U_c$  increases from 0.5 to 1.5, the corresponding average velocity of the microbubbles tip  $L_t$  growth increases from  $1.29 \mu\text{m}/\mu\text{s}$  to  $3.31 \mu\text{m}/\mu\text{s}$ . It can be concluded that the  $L_t$  of the bubbles at the time of bubbles breakage increases with the increase in the flow rate of the dispersed phase. When the dispersed-phase flow rate increases, the generation period of microbubbles increases, and therefore, the final length of microbubbles also increases. From Fig. 10(c), it is concluded that the tip growth rate is basically the same at  $0.5\text{--}1.25 \mu\text{s}$ , and the larger the continuous phase flow rate is, the larger the average rate of tip growth is as time increases. During the necking and quick break stages, the downstream flow of microbubbles is mainly driven by the continuous phase and shear

**Fig. 9** Evolution of tip length  $L_t$  and neck width  $W_n$  during microbubbles formation in the plugging regime



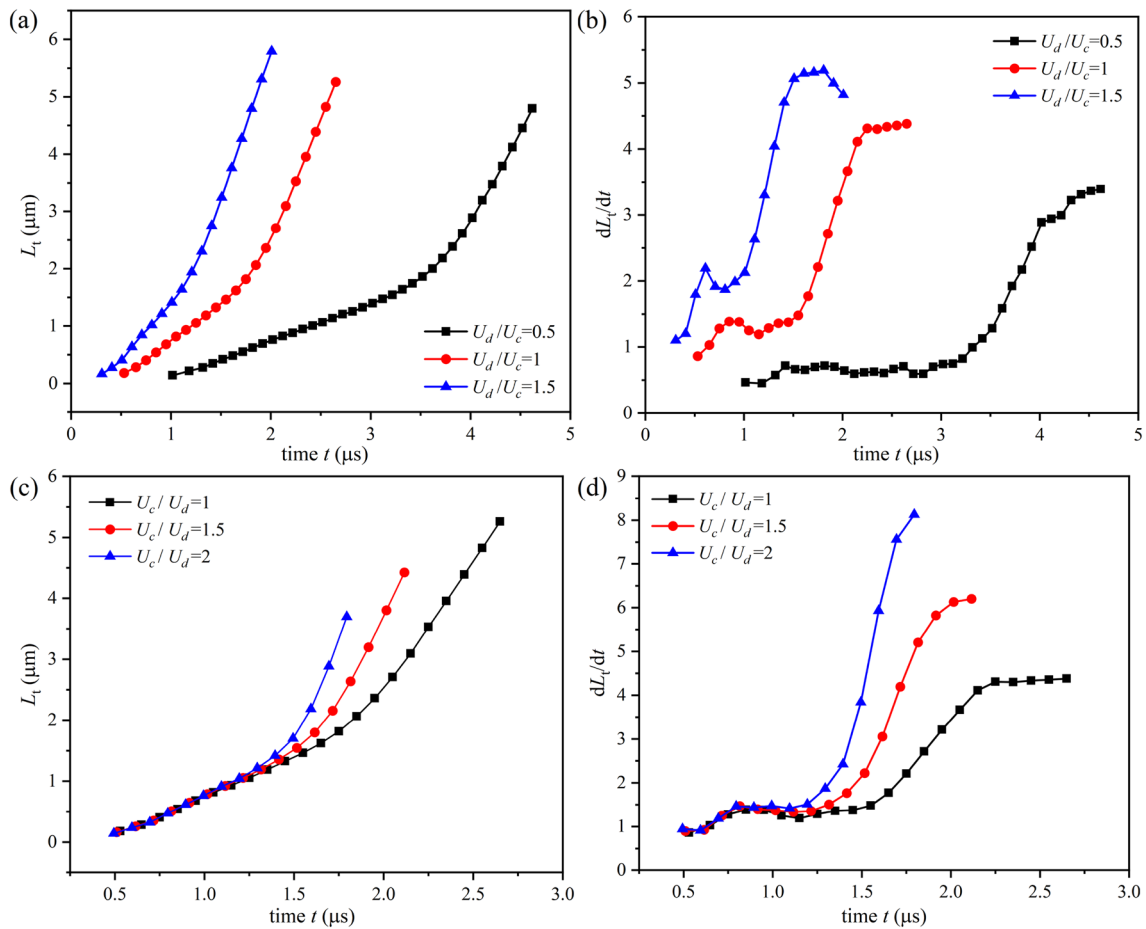


**Fig. 10** (a) Effect of varying the dispersed-phase flow rate on the tip length  $L_t$ ; (b) Effect of varying the dispersed phase flow rate on the temporary evolution of the tip velocity  $dL_t/dt$ ; (c) Effect of varying

the continuous phase flow rate on the tip length  $L_t$ ; (d) Effect of varying the continuous phase flow rate on the temporary evolution of the tip velocity  $dL_t/dt$

has little effect on the movement of microbubbles. During the expanding phase, the shear force acts mainly as a stretch at the microbubbles tip.

The temporary evolution of the gas flow tip rate for a given continuous phase velocity is shown in Fig. 10(b). In the first stage, the gas stream is formed by the gas phase, which flows at a velocity  $U_d$ . The liquid in orifice slightly accelerates the initial tip formation. In the second stage, the liquid flow becomes significantly obstructed, the liquid squeezes the gas flow and the gas flow undergoes a large acceleration before approaching the rapid fracture stage. It is also obvious from this phenomenon that the formation of bubbles at the orifice is mainly controlled during the necking phase, which is mainly controlled by the liquid flow rate. The maximum value of the rate of change of  $L_t$  is 3.39 when  $U_d/U_c=0.5$  and 5.16 when  $U_d/U_c=1.5$ , which can be concluded that the higher the flow rate of the dispersed phase, the higher rate of change of  $L_t$ .

Figure 10(d) shows the temporary evolution of gas flow tip rate for a certain velocity of dispersed phase. When the

velocity of dispersed phase is constant and the velocity of continuous phase varies, the trend of gas flow tip is essentially constant in the early stages. Later it is observed that as the velocity of continuous phase increases, the rate of tip formation becomes faster and slows down when the neck is about to break. The maximum value of the rate of change of  $L_t$  is 4.38 when  $U_c/U_d=1$  and 8.13 when  $U_c/U_d=2$ . It can be concluded that the higher the velocity of the continuous phase, the higher the tip velocity, which slows down when the neck is about to break.

Figure 11 represents the effect of the change in flow rate of the two phases on the neck width ( $W_n$ ) during microbubble forming. From Fig. 11(a), it can be seen that in the case of the continuous phase flow rate is fixed, changing the flow rate of the dispersed phase, the change trend of the neck width in the formation process of microbubbles is basically unchanged, and the length of time used to reach the same neck width is inversely proportional to the flow rate of the dispersed phase, the greater flow rate of the dispersed phase is, the time used to reach the same neck width is shorter, and

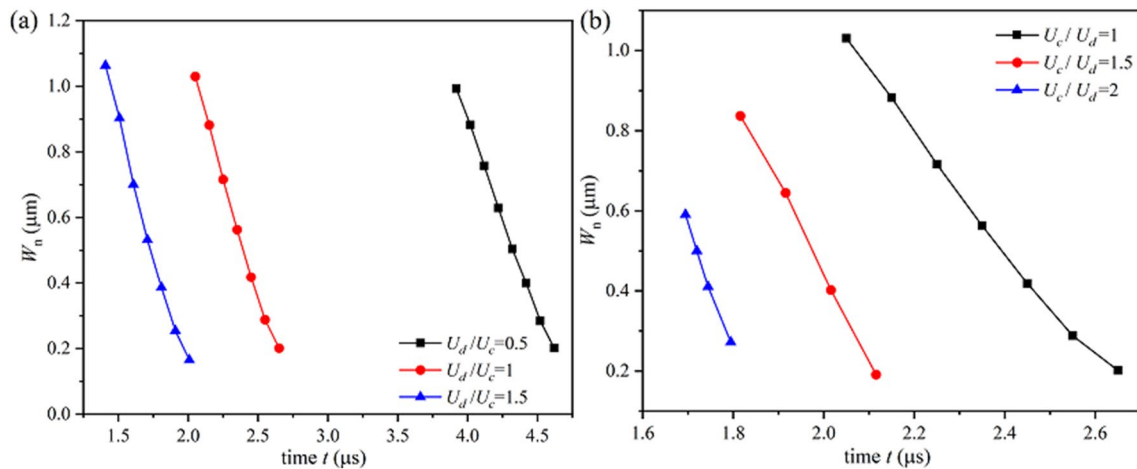


**Fig. 11** Effect of two-phase flow rate on microbubbles formation: (a) effect of dispersed phase flow rate on  $W_n$ ; (b) effect of continuous phase flow rate on  $W_n$

the corresponding increase in the frequency of the formation of microbubbles. Meanwhile, at the same dispersed-phase velocity, the time used was  $0.7 \mu\text{s}$  when the flow rate ratio was 0.5,  $0.60008 \mu\text{s}$  and  $0.6 \mu\text{s}$  when the flow rate ratios were 1 and 1.5, respectively, with little difference in the necking time. As can be seen in Fig. 11(b), with a constant flow rate of the dispersed phase, the trend of the neck width changes slowly as flow rate of the continuous phase decreases. When  $U_c/U_d=2$ , the necking velocity is  $3.91 \mu\text{m}/\mu\text{s}$ , and when  $U_c/U_d=1$ , the necking velocity is  $1.382 \mu\text{m}/\mu\text{s}$ . The necking velocity is enhanced by 64 %, which is attributed to the increased flow rate in the continuous phase, and the increase in the liquid momentum will pinch the neck of the gas flow more quickly and shorten the necking time.

### The Effect of Continuous Phase Viscosity

In this section the effect of continuous phase viscosity ( $\mu_c$ ) on the diameter and frequency of microbubbles is investigated separately. Three groups of parameters (1.0 mPa·s, 1.5 mPa·s, 2.0 mPa·s) were selected for the calculation of continuous phase viscosity for the simulation, where the viscosity of dispersed phase was fixed at  $0.01663 \text{ mPa}\cdot\text{s}$  and the ratio of the two phase flow rates was  $U_d/U_c=0.2$ .

Figure 12 shows the effect of continuous phase viscosity on the diameter of microbubbles and the formation frequency. It can be seen that the continuous phase viscosity ( $\mu_c$ ) has a significant effect on the size of the microbubbles which are formed. Increasing the viscosity of continuous phase results in greater resistance, which leads to faster microbubbles formation and a decrease in microbubbles diameter. As the viscosity of continuous phase increases from 1.0 mPa·s to 2.0 mPa·s, the diameter of microbubbles decreases from  $1.6949 \mu\text{m}$  to  $1.4339 \mu\text{m}$ ; the frequency of

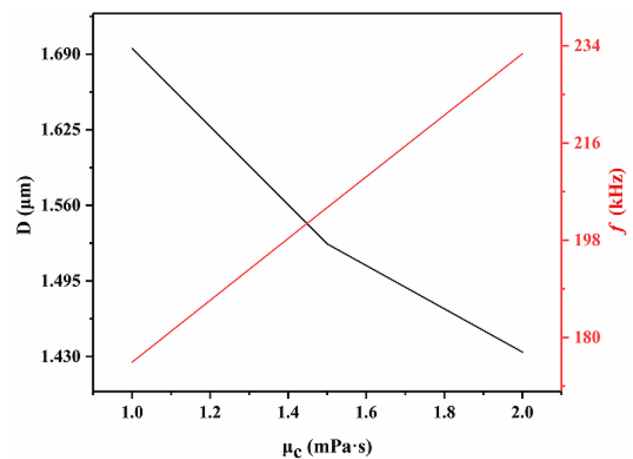


**Fig. 12** Effect of varying continuous phase viscosity ( $\mu_c$ ) on microbubble diameter and formation frequency

microbubbles formation increases from  $175.438 \text{ kHz}$  to  $232.558 \text{ kHz}$ . The increase of the continuous phase viscosity leads to higher inertial force exerted near the orifice of dispersed phase, faster rupture of the gas tip and then small size bubbles are produced. On the other hand, reducing the viscosity of continuous phase means that the effect of shear forces is weakened, making the break-up of the gas tip somewhat more difficult, so that the time required for the first bubble to form grows as its size increases.

Figure 13 shows the evolution of the microbubble tip at different viscosities, the dashed line indicates the moment when the necking begins. As can be seen from the figure, the change in viscosity has very little effect on the tip of the microbubbles at the beginning, and as the gas flow continues to enter, the trend in the evolution of the tip changes before the contraction phase of the neck begins. After

entering the necking stage, the growth trend of microbubbles tip increases with the viscosity increasing, the growth rate of microbubbles tip is  $2.13 \mu\text{m}/\mu\text{s}$  when  $\mu = 1 \text{ mPa}\cdot\text{s}$ , and  $2.782 \mu\text{m}/\mu\text{s}$  when  $\mu = 2 \text{ mPa}\cdot\text{s}$ . The results show that the higher the viscosity, the faster the change tendency, which means that the breakage point is reached more quickly, and the frequency of formation of microbubbles is also faster. The results show that the higher the viscosity, the faster the change trend, which also indicates that the breakage point is reached faster, and the frequency of microbubbles formation is also faster.

Figure 14 illustrates the variation of pressure at different locations in the channel with time for different viscosities, where Fig. 14(a) shows the pressure drop variation between the upstream and downstream of the orifice, it's the pressure

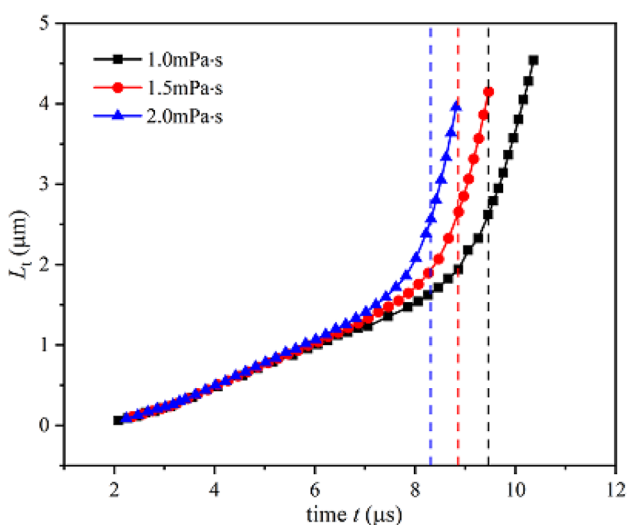


Fig. 13 Evolution of microbubbles tip at different continuous phase viscosity

variation at point *d* and point *p*. The pressure shows a cyclical variation with time. The higher the viscosity, the higher the pressure drop at the initial moment, which also decreases first, that is because the larger viscosity leads to faster formation of microbubbles, and the different continuous phase viscosities remain essentially the same at the lowest smooth pressure drop. As shown in Fig. 14(b), the variation of  $P_c$  with viscosity is observed by plotting the pressure diagram for different continuous phase viscosities. When the dispersed phase first starts to enter the orifice, the resistance of continuous phase remains essentially constant and the variation of  $P_c$  is not significant. It can be observed that the higher that the viscosity is, the greater will be the  $P_c$  at the first moments. When the dispersed phase continues to enter the orifice, the pressure at the inlet of continuous phase gradually increases. The higher viscosity of continuous phase causes the neck of dispersed phase to start shrinking faster and reach a maximum value of  $P_c$ . After the neck rupture,  $P_c$  suddenly decreases and then the periodic circulation begins. Although the higher of continuous phase viscosity, the  $P_c$  becomes greater, the  $P_c$  evolution remains essentially the same throughout.

### The Effect of Wall Wettability

Wettability of the wall surface is a key factor when bubbles are formed or moving within a microchannel, as it affects the microbubbles formation mechanism, size and formation frequency. The magnitude of the wall contact angle is used in the simulation to indicate wettability, so this section investigates the effect of contact angle ( $\theta$ ) on microbubbles diameter (*D*), formation frequency (*f*) and interface evolution. Three sets of contact angle parameters ( $0^\circ, 50^\circ, 90^\circ$ ) were selected for the calculations, where the continuous

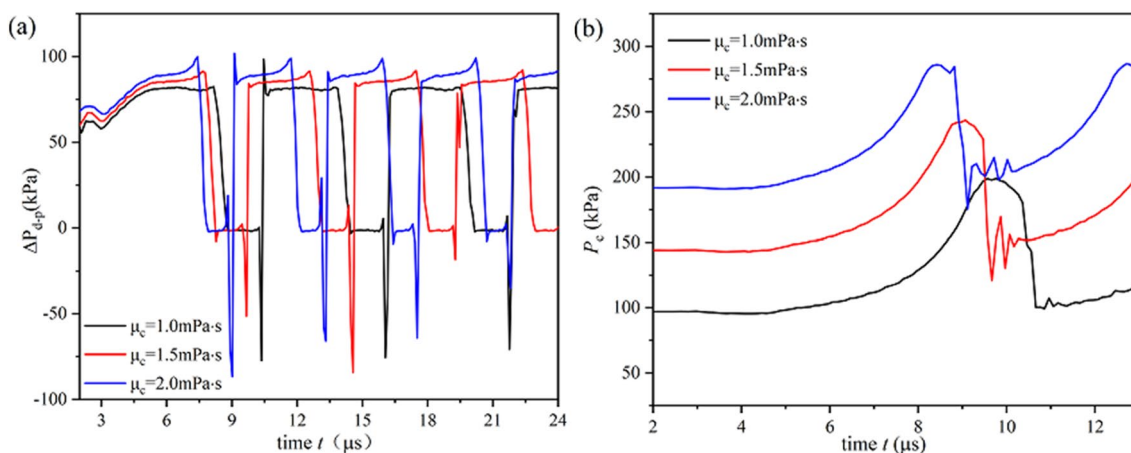


Fig. 14 Pressure variation with viscosity at different positions in the channel: (a) pressure drop variation from point *d* to point *p*; (b) pressure variation  $P_c$  with viscosity at position *c* at the continuous phase inlet

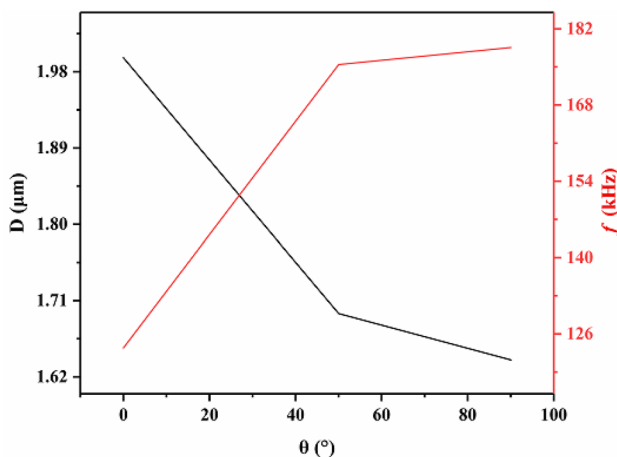


phase flow rate is 1.0 m/s and the dispersed phase flow rate is 0.2 m/s.

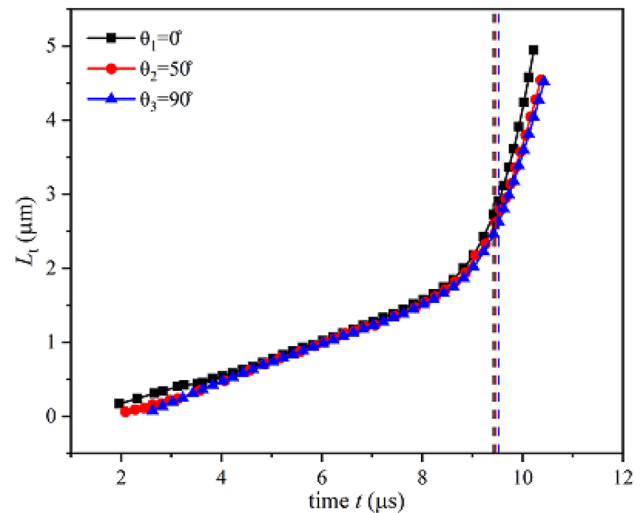
As the contact angle increases, the diameter of the microbubbles decreases. This is because the adhesion on the wall decreases as the contact angle increases, leading to a reduction in general flow resistance, which facilitates the formation of microbubbles. As the contact angle increases from  $0^\circ$  to  $90^\circ$ , the microbubbles diameter reduces from  $1.9966 \mu\text{m}$  to  $1.6402 \mu\text{m}$  and the generation frequency increases from 123.456 kHz to 178.571 kHz. Figure 15 shows the effect of contact angle on microbubbles diameter and formation frequency.

Figure 16 shows the evolution of microbubbles tip at different contact angles, with the dashed line indicating the moment when the neck starts to shrink. In the pre-growth stage, the growth rate is  $0.1486 \mu\text{m}/\mu\text{s}$  when  $\theta = 0^\circ$  and  $0.287 \mu\text{m}/\mu\text{s}$  when  $\theta = 90^\circ$ , which indicates that the larger the contact angle is, the larger the growth trend of the microbubbles tip is. In the middle growth stage, the tendency of different contact angles is not significant and basically in the same tendency. In the late growth stage, the larger the contact angle, the later the start of the necking stage, calculations show that when  $\theta = 0^\circ$ , the growth rate of  $2.907 \mu\text{m}/\mu\text{s}$ , when  $\theta = 90^\circ$ , the growth rate of  $2.15 \mu\text{m}/\mu\text{s}$ , the growth tendency of the necking stage is the opposite of the growth stage in the early stage, showing a tendency for smaller contact angles and greater changes in microbubbles tip growth, thus the smaller contact angle in the necking stage can speed up the microbubbles growth. Therefore, a smaller contact angle in the necking stage can accelerate the breakage generation of microbubbles.

The velocity vector and phase interface before the microbubbles break up at different contact angles, as shown in Fig. 17. At the inlet of dispersed phase, the velocity vector circulation zone is formed. The circulation zone is more



**Fig. 15** Effect of wall contact angle on microbubbles diameter and formation frequency



**Fig. 16** Tip evolution of microbubbles at different contact angles

clearly shown when the contact angle is  $90^\circ$ . When  $\theta = 0^\circ$ , the continuous phase enters the dispersed phase inlet due to the hydrophilic properties of wall and the microbubbles head lengthens, leading to increasing bubble size and formation frequency decreases. When  $\theta = 50^\circ$ , the breakup rate of bubbles neck increases. At the point where the neck of gas flow will break, the neck velocity increases and the velocity at microbubbles tip interface is greater than the velocity at the internal center. When  $\theta = 90^\circ$ , the continuous phase does not enter the dispersed phase, but the circulation zone near orifice does not disappear. When the neck is about to be broken, the velocity of the neck is larger, and the velocity of the microbubble tip interface is larger compared to the velocity of the inner center.

Figure 18 describes the pressure variation at different locations of the channel at different contact angles, including the pressure difference variation from point d to point p and the pressure variation at c with time. From Fig. 18(a), it can be seen that the value of pressure variation in one period is essentially constant. When  $\theta$  is  $0^\circ$ , there is a continuous phase flow into the inlet of the dispersed phase, resulting in a different pressure variation in the necking phase than when the contact angle is  $50^\circ$  and  $90^\circ$ . Therefore microbubbles are formed in a stable manner and a smaller contact angle cannot be chosen. As shown in Fig. 18(b), the sensitivity of pressure at point c in the continuous phase channel to the hydrophilicity of wall can be seen by plotting the pressure at different contact angles. It is observed that for the value of  $\theta$  in the figure, the pressure in the growth phase hardly changes, which is due to the constant flow rate. As the continuous phase enters the orifice and is resisted by the dispersed phase, the pressure starts to gradually become larger. The neck of the microbubbles starts to shrink and the pressure then decreases continuously. When  $\theta$  is  $0^\circ$ , as the

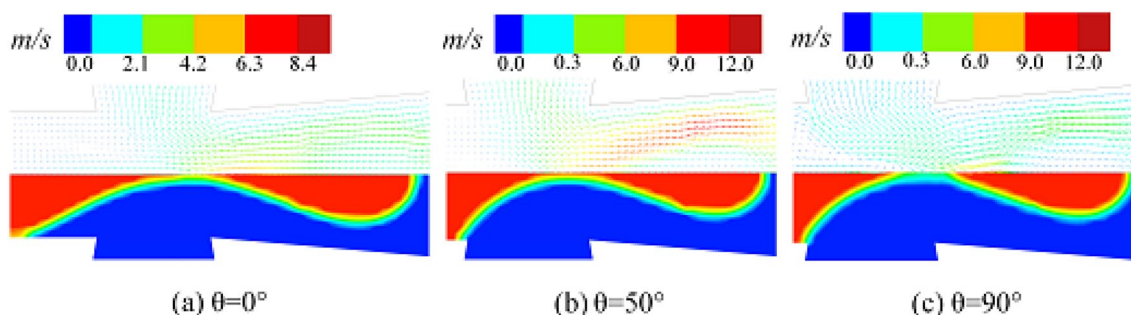


Fig. 17 Velocity field and phase interface before microbubbles breakup for different contact angles ( $\theta$ ).

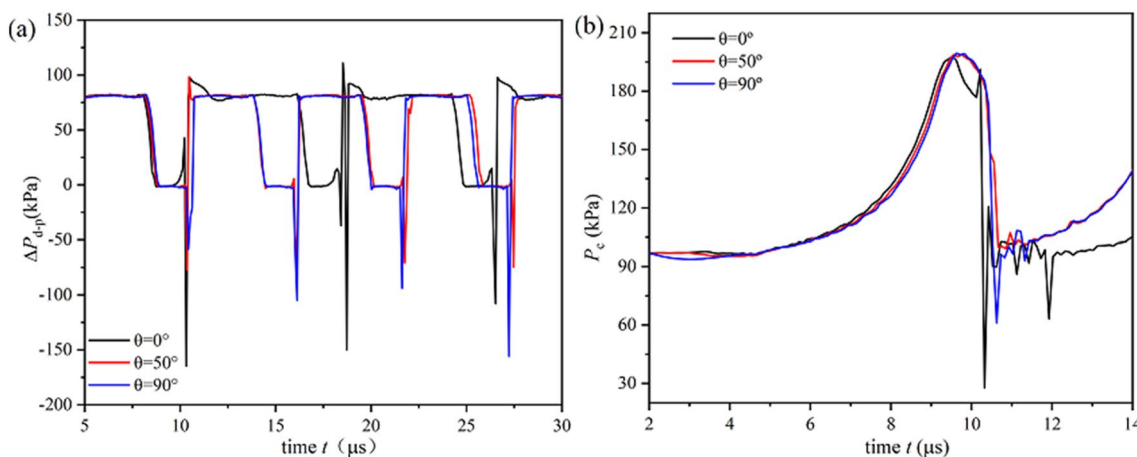


Fig. 18 Evolution of pressure with contact angle ( $\theta$ ) at different positions in the channel: (a) variation of pressure drop from point  $d$  to point  $p$ ; (b) evolution of pressure  $P_c$  with contact angle at position  $c$  of continuous phase inlet

continuous phase enters the dispersed phase channel from the wall, the neck breaks to form microbubbles and the dispersed phase continuously enters the orifice. In contrast,  $P_c$  increases slowly at  $\theta$  of  $0^\circ$ , while it does not change much at  $\theta$  of  $50^\circ$  and  $90^\circ$ .

### The Effect of Interfacial Tension

Interfacial tension corresponds to the minimum “reversible” force that must be provided to remove molecules (connected to each other by cohesive forces) from the core of a material or from another phase on its surface, thereby deforming it. When two immiscible fluids come into contact, interfacial tension stabilizes the balance between the two phases, which makes it possible to balance the forces exerted at the interface. However, the more interfacial tension is applied, the greater the energy required to overcome it and the more difficult it is to produce bubbles, and it can be argued that interfacial tension is the only conservative force preventing bubbles from breaking. However, the velocity applied to the liquid inlet forces the gas line through the orifice into the outlet channel to break the small bubbles and shrink back upstream, the process is then

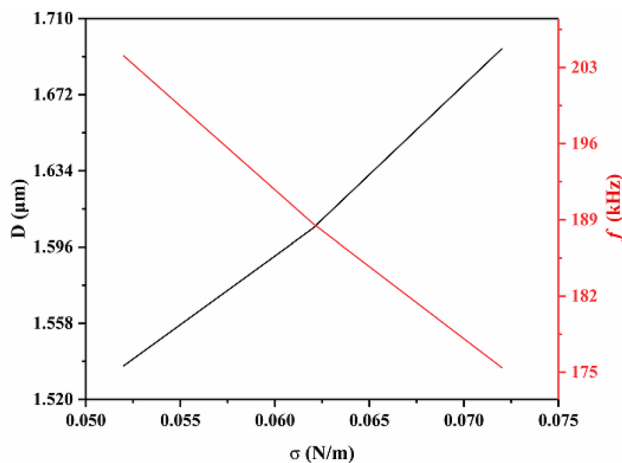
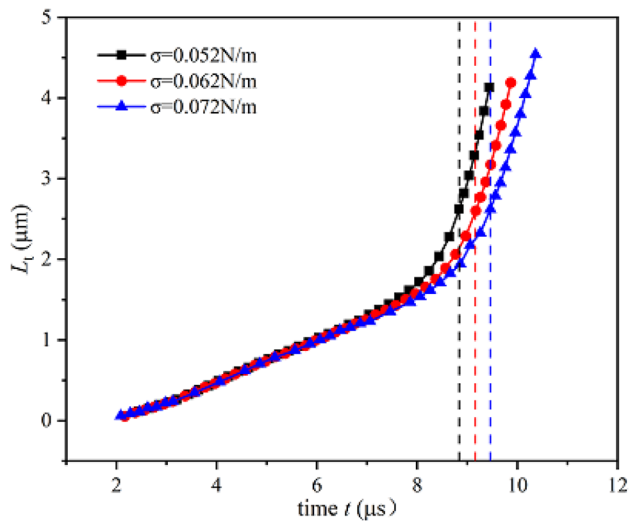


Fig. 19 The effect of interfacial tension on microbubbles diameter and formation frequency

repeated. Three sets of interfacial tension values (0.052 N/m, 0.062 N/m, 0.072 N/m) are set in this section to investigate the effect of interfacial tension on microbubbles formation.



**Fig. 20** Evolution of the microbubbles tip with time for different interfacial tension

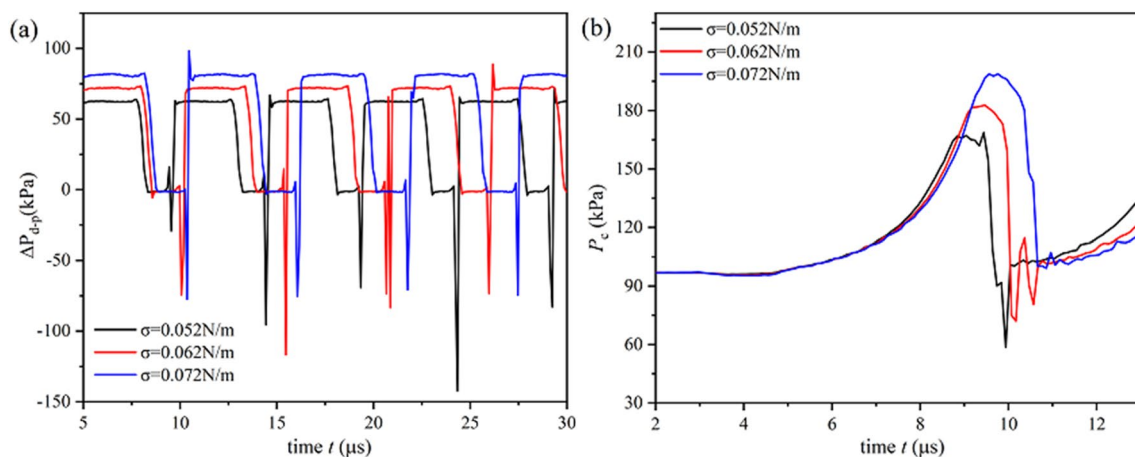
The continuous phase flow rate was set at 1.0 m/s and the dispersed phase flow rate at 2.0 m/s.

Figure 19 represents the variation of microbubbles diameter and formation frequency with interfacial tension. Increasing the interfacial tension increases the cohesion between molecules on the surface of the airflow tip and makes it more difficult to achieve force equilibrium, resulting in a reduction in the shear stress required to dominate the fracture tip at the interface, slower bubbles formation and therefore larger microbubbles size. As the interfacial tension increases from 0.052 N/m to 0.072 N/m, the microbubbles diameter increases from 1.5368  $\mu\text{m}$  to 1.6949  $\mu\text{m}$  and the forming frequency decreases from 204.081 kHz to 175.438 kHz. This can be interpreted as an increase in interfacial tension and

a decrease in Ca number, indicating an increase in the time required for phase interface fracture.

Figure 20 shows the evolution of the microbubbles tip at different viscosities, with the dashed line indicating the moment of onset of necking. From the Fig. 20, it can be seen that with the increasing interfacial tension, the change tendency of microbubble tip growth in the pre-stage and middle stage is basically the same, and the growth rate is the same as 0.24  $\mu\text{m}/\mu\text{s}$ . After entering the necking stage, the microbubbles tip growth rate is 2.513  $\mu\text{m}/\mu\text{s}$  when  $\sigma = 0.052$  N/m, and the microbubbles tip growth rate is 2.13  $\mu\text{m}/\mu\text{s}$  when  $\sigma = 0.072$  N/m. The results indicate that the microbubbles tip growth changes more rapidly with small interfacial tension, which promotes faster breakage and generation of the microbubbles, the results show that the change of microbubbles tip growth is faster for small interfacial tension, which promotes faster breakage generation of microbubbles.

Figure 21 describes the variation of pressure with interfacial tension ( $\sigma$ ) at different locations, including the pressure change from point *d* to point *p* and the pressure change with time at the continuous phase channel *c*. As seen in Fig. 21(a), the maximum pressure drop during the period is high with increasing interfacial tension, while slowing down the process of pressure drop variation. The smooth zone of the lowest pressure drop remains essentially constant during the periodic variation at different interfacial tensions. As shown in Fig. 21(b), the pressure at position *c* in the continuous phase flow can be seen to be influenced by the interfacial tension by plotting the pressure at different interfacial tensions. As the interfacial tension decreases, the smaller the maximum value of  $P_c$  and the earliest the maximum pressure is attained, after which it also decreases to a minimum in a relatively short period of time.



**Fig. 21** Evolution of pressure with interfacial tension ( $\sigma$ ) at different positions in the channel: (a) variation of pressure drop from point *d* to point *p*; (b) evolution of pressure  $P_c$  with interfacial tension at position *c* of continuous phase inlet

## Conclusion

This paper investigates the formation of microbubbles in flow-focused microchannels and draws preliminary conclusions on the effect of each parameter on the formation of microbubbles. The main conclusions are as follows:

- (1) As the velocity of the two phases changes, the bubbles in channel appear in three flow regimes: dripping regime, plugging regime and threading regime. The dripping regime is the most widespread of these. When  $U_d$  is high, the microbubbles flow in a tandem state in the channel. When  $U_c$  is small, the bubbles are in the microchannel in the plugging regime. The microbubbles in the plugging regime come into contact with the channel walls and move along walls towards the outlet. The dripping regime sometimes produces satellite bubbles, but they merge with the main bubbles downstream. The large inertia of the dispersed phase in threading regime suppresses the effect of interfacial tension and thus the Rayleigh-Plateau instability.
- (2) The tip distance of the gas phase flow shows a non-linear increase with time. The time of neck shrinkage in the plugging regime accounts for a high proportion of the overall bubbles formation process. The formation of plugging regime at the orifice is mainly controlled by the neck shrinkage phase. The higher the continuous phase flow rate, the faster the change of the microbubbles tip when the dispersed phase flow rate is certain; when the continuous phase flow rate is certain, the change of the microbubbles tip growth phase is not significantly influenced by the dispersed phase flow rate. At a constant dispersed phase flow rate, and the lower the continuous phase flow rate, the faster the rate of change in neck width, and the increase in liquid momentum will entrap the neck of the gas flow more quickly and accelerate the necking of the gas flow.
- (3) By increasing the viscosity of continuous phase, the frequency of microbubbles formation increases and the diameter decreases. As the wall contact angle decreases, the adhesion of the continuous phase to the channel walls at the microchannel crossings increases, resulting in a longer time for the microbubbles to detach from the dispersed phase. With the velocity of dispersed phase remaining constant, the size of the microbubbles increases due to the accumulation of more dispersed phase. The increase in surface tension causes the cohesion between molecules on the surface of gas flow to increase and makes it more difficult to achieve force equilibrium, resulting in slower bubbles formation and therefore larger microbubbles diameters as the surface dominates the shear stress required to break the gas flow.

**Acknowledgements** We gratefully acknowledge the supports of the Open Foundation of the State Key Laboratory of Fluid Power and Mechatronic Systems (GZKF-202122), the Independent Innovation Projects of the Hubei Longzhong Laboratory (2022ZZ-14) and the National Natural Science Foundation of China (51875419).

**Data availability** The authors confirm that the data supporting the findings of this study are available within the article.

## Declarations

**Conflict of Interest** The authors report there is no competing interests to declare.

## References

1. A.J. Dixon, J.M.R. Rickel, B.D. Shin, A.L. Klibanov, J.A. Hosack, In vitro sonothrombolysis enhancement by transiently stable microbubbles produced by a flow-focusing microfluidic device. *Ann. Biomed. Eng.* **46**, 222–232 (2018)
2. C. Liu, X. Chen, J. Zhang, H. Zhou, L. Zhang, Y. Guo, Advanced treatment of bio-treated coal chemical wastewater by a novel combination of microbubble catalytic ozonation and biological process. *Sep. Purif. Technol. Purif. Technol.* **197**, 295–301 (2018)
3. A.S. Reis, M.A.S. Barrozo, A study on bubble formation and its relation with the performance of apatite flotation. *Sep. Purif. Technol. Purif. Technol.* **161**, 112–120 (2016)
4. X. Wang, S. Yuan, J. Liu, Y. Zhu, Y. Han, Nanobubble-enhanced flotation of ultrafine molybdenite and the associated mechanism. *J. Mol. Liq.* **346**, 118312 (2022)
5. A. Rahman, D.A. Khodadadi, M. Abdollahy, M. Fan, Nano-microbubble flotation of fine and ultrafine chalcopyrite particles. *Int. J. Min. Sci. Techno.* **24**(4), 559–566 (2014)
6. N. Wang, H. Lu, X. Xu, Y. Liu, Y. Li, F. Yuan, Q. Yang, Enhanced oil removal from oily sand by injecting micro-macro-bubbles in swirl elution. *J. Environ. Manage.* **316**, 115175 (2022)
7. S. Shi, N. Oono, S. Ukai, T. Ishida, M. Ohnuma, Dispersion and strength parameter of nano-sized bubbles in copper investigated by means of small-angle X-ray scattering and transmission electron microscopy. *Mat. Sci. Eng. A-struct* **658**, 296–300 (2016)
8. H. Xiao, S. Geng, A. Chen, C. Yang, F. Gao, T. He, Q. Huang, Bubble formation in continuous liquid phase under industrial jetting conditions. *Chem. Eng. Sci.* **200**, 214–224 (2019)
9. J.A. Hammons, S.J. Tumey, Y. Idell, J.R. Jeffries, He bubble concentration, size and strain in implanted aluminum by SAXS/WAXS. *JOM* **72**, 176–186 (2020)
10. J.P. Christiansen, B.A. French, L. Klibanov, S. Kaul, J.R. Lindner, Targeted tissue transfection with ultrasound destruction of plasmid-bearing cationic microbubbles. *Ultrasound Med. Biol.* **29**, 1759–1767 (2003)
11. J.B. Freund, Suppression of shocked-bubble expanding due to tissue confinement with application to shock-wave lithotripsy. *J. Acoust. Soc. Am. Acoust. Soc. Am.* **123**, 2867–2874 (2008)
12. Y. Zhao, H. Liang, X. Mei, M. Halliwell, Preparation, characterization and in vivo observation of phospholipid-based gas-filled microbubbles containing hirudin. *Ultrasound Med. Biol.* **31**, 1237–1243 (2005)
13. K. Soetanto, M. Chan, Fundamental studies on contrast images from different-sized microbubbles: analytical and experimental studies. *Ultrasound Med. Biol.* **26**, 81–91 (2000)
14. T. Fu, Y. Wu, Y. Ma, H. Li, Droplet formation and breakup dynamics in microfluidic flow-focusing device: from dripping to jetting. *Chem. Eng. Sci.* **84**, 207–217 (2012)

15. U. Farook, E. Stride, M.J. Edirisinghe, R. Moaleji, Microbubbling by co-axial electrohydrodynamic atomization. *Med. Biol. Eng. Comput.* **45**, 781–789 (2007)
16. J. Zhou, A.V. Ellis, N.H. Voelcker, Recent developments in pdms surface modification for microfluidic devices. *Electrophoresis* **31**, 2–16 (2010)
17. E. Stride, M. Edirisinghe, Novel preparation techniques for controlling microbubble uniformity: a comparison. *Med. Biol. Eng. & Comput.* **47**, 883–892 (2009)
18. H. Peng, Z. Xu, S. Chen, L.B. Zhang, L. Ge, An easily assembled double T-shape microfluidic devices for the preparation of submillimeter-sized polyacrylonitrile (PAN) microbubbles and polystyrene (PS) double emulsions. *Colloid. Surface. A.* **468**, 271–279 (2015)
19. J. Xu, S. Li, Y. Wang, G. Luo, Controllable gas-liquid phase flow patterns and monodisperse microbubbles in a microfluidic T-junction device. *Appl. Phys. Lett.* **88**, 133506 (2006)
20. E. Lorenceau, Y.Y.C. Sang, R. Höhler, S. Cohen-Addad, A high rate flow-focusing foam generator. *Phys. Fluids* **18**, 097103 (2006)
21. B. Dollet, W. van Hoeve, J.P. Raven, P. Marmottant, M. Versluis, Role of the channel geometry on the bubble pinch-off in flow-focusing devices. *Phys. Rev. Lett.* **100**, 034504 (2008)
22. W. Yu, X. Liu, B. Li, Y. Chen, Experiment and prediction of droplet formation in microfluidic cross-junctions with different bifurcation angles. *Int. J. Multiphas. Flow* **149**, 103973 (2022)
23. E. Roumpea, N.M. Kovalchuk, M. Chinaud, E. Nowak, M.J.H. Simmons, P. Angeli, Experimental studies on droplet formation in a flow-focusing microchannel in the presence of surfactants. *Chem. Eng. Sci.* **195**, 507–518 (2019)
24. J. Huang, Z. Yao, Influencing factors and size prediction of bubbles formed by flow focusing in a cross-channel. *Chem. Eng. Sci.* **248**, 117228 (2022)
25. W. Han, X. Chen, Z. Wu, Y. Zheng, Three-dimensional numerical simulation of droplet formation in a microfluidic flow-focusing device. *J. Braz. Soc. Mech. Sci.* **41**, 1–10 (2019)
26. S.G. Sontti, A. Atta, Numerical insights on controlled droplet formation in a microfluidic flow-focusing device. *Ind. Eng. Chem. Res.* **59**, 3702–3716 (2019)
27. D. Pan, M. Liu, Q. Chen, W. Huang, B. Li, Effects of channel sizes on traffic of solid in water in oil compound droplets through a vertical channel. *J. Disper. Sci. Technol.* **40**, 537–545 (2019)
28. I.-L. Ngo, T.-D. Dang, C. Byon, S.W. Joo, A numerical study on the dynamics of droplet formation in a microfluidic double T-junction. *Biomicrofluidics* **2**, 024107 (2015)
29. M. Hashimoto, S. S. Shevkoplyas, Zasońska Beata, S. Tomasz, G. Piotr and W. George, Formation of bubbles and droplets in parallel, coupled flow-focusing geometries. *Small*, **10**, 1795–1805 (2010)
30. S. Mi, C. Zhu, Y. Ma, T. Fu, Bubble formation in high-viscosity liquids in step-emulsification microdevices. *J. Ind. Eng. Chem.* **114**, 221–232 (2022)
31. Z. Zhang, S. Jiang, C. Zhu, Y. Ma, T. Fu, Bubble formation in a step-emulsification microdevice with parallel microchannels. *Chem. Eng. Sci.* **224**, 115815 (2020)
32. Z. Zhang, Z. Wang, F. Bao, M. Fan, S. Jiang, C. Zhu, Y. Ma, T. Fu, Bubble formation in a step-emulsification microdevice: hydrodynamic effects in the cavity. *J. Ind. Eng. Chem.* **94**, 127–133 (2020)
33. W. Zhan, Z. Liu, S. Jiang, C. Zhu, Y. Ma, T. Fu, Comparison of formation of bubbles and droplets in step-emulsification microfluidic devices. *J. Ind. Eng. Chem.* **106**, 469–481 (2022)
34. P. Ma, T. Fu, C. Zhu, Y. Ma, Asymmetrical breakup and size distribution of droplets in a branching microfluidic T-junction. *Korean J. Chem. Eng.* **36**, 21–29 (2019)
35. Z. Wang, W. Ding, Y. Fan, J. Wang, J. Chen, H. Wang, Design of improved flow-focusing microchannel with constricted continuous phase inlet and study of fluid flow characteristics. *Micromachines* **13**, 1776 (2022)
36. W. Yu, X. Liu, Y. Zhao, Y. Chen, Droplet generation hydrodynamics in the microfluidic cross-junction with different junction angles. *Chem. Eng. Sci.* **203**, 259–284 (2019)
37. J.U. Brackbill, D.B. Kothe, C. Zemach, A continuum method for modeling surface tension. *J. Com. Phys.* **100**, 335–354 (1992)
38. T. Fu, D. Funfschilling, Y. Ma, H. Li, Scaling the formation of slug bubbles in microfluidic flow-focusing devices. *Microfluid. Nanofluid.* **8**, 467–475 (2010)

**Publisher's Note** Springer Nature remains neutral with regard to jurisdictional claims in published maps and institutional affiliations.

Springer Nature or its licensor (e.g. a society or other partner) holds exclusive rights to this article under a publishing agreement with the author(s) or other rightsholder(s); author self-archiving of the accepted manuscript version of this article is solely governed by the terms of such publishing agreement and applicable law.